Hydrothermally Tailored Three-Dimensional Ni−V Layered Double Hydroxide Nanosheets as High-Performance Hybrid Supercapacitor Applications

Ankit Tyagi,[†] Manish Chandra Joshi,[†] Asmita Shah,[†] Vijay Kumar Thakur,[§] and Raju Kumar Gupta*,[†,‡]

[†]Department of Chemical Engineering and [‡]Center for Environmental Science and Engineering, Indian Institute of Technology Kanpur, Kanpur 208016, UP, India

[§]School of Aerospace, Transport and Manufacturing, Enhanced Composites and Structures Center, Cranfield University, College Road, Cranfield MK43 0AL, Bedfordshire, United Kingdom

S *Supporting Information*

ABSTRACT: Here, we report a facile and easily scalable hydrothermal synthetic strategy to synthesize Ni−V layered double hydroxide (NiV LDH) nanosheets toward high-energy and high-power-density supercapacitor applications. NiV LDH nanosheets with varying Ni-to-V ratios were prepared. Three-dimensional curved nanosheets of $Ni_{0.80}V_{0.20}$ LDH showed better electrochemical performance compared to other synthesized NiV LDHs. The electrode coated with $Ni_{0.80}V_{0.20}$ LDH nanosheets in a three-electrode cell configuration showed excellent pseudocapacitive behavior, having a high specific capacity of 711 C g^{-1} (1581 F g^{-1}) at a current density of 1 A g^{-1} in 2 M KOH. The material showed an excellent rate capability and retained the high specific capacity of 549 C g^{-1} (1220 F g^{-1}) at a current density of 10 A g^{-1} and low internal resistances. Owing to its superior performance, $Ni_{0.80}V_{0.20}$ LDH nanosheets were used as positive electrode and commercial activated carbon was used as negative electrode for constructing a hybrid supercapacitor (HSC) device, having a working voltage of 1.5 V. The HSC device exhibited a high specific capacitance of 98 F g^{-1} at a current density of 1 A g^{-1}. The HSC device showed a higher energy density of 30.6 Wh kg^{-1} at a power density of 0.78 kW kg^{-1} and maintained a high value of 24 Wh kg^{-1} when the power density was increased to 11.1 kW kg^{-1}. The performance of NiV LDHs nanosheets indicates their great potential as low-cost electrode material for future energy-storage devices.
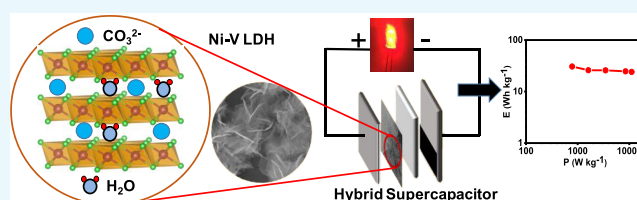
1. INTRODUCTION

Due to global economy development, the continuous upsurge in demand of energy gives rise to the excessive consumption of fossil fuels, which eventually has resulted in lessening of fossil fuels, environmental pollution, and global warming.[1,2] To safeguard the environment from adverse impacts and meet the future energy demand, electricity generated through clean route has gained increased attention, which is one of the major thrust areas in renewable energy.[3,4] Supercapacitors, also known as ultracapacitors, are one of the safe and attractive energy-storage devices over batteries and conventional capacitors due to their higher power density than batteries and higher energy density compared to conventional dielectric capacitors.[5] On the basis of charge-storage mechanisms, supercapacitors are classified as electric double-layer capacitors (EDLCs) and pseudocapacitors.[6] In EDLCs, charge is stored due to electrostatic attraction between electrolyte ions at the electrode−electrolyte interface; however, charge-storage mechanism follows a Faradic reaction, i.e., charge storage takes place at the surface of active electrode material in pseudocapacitors.[7] Pseudocapacitors, due to their higher energy density and specific capacitance compared to EDLCs, are more attractive

candidates for future energy-storage devices.[8] Transition-metal oxides like Co_3O_4,[9] MnO_2,[10] RuO_2,[11] TiO_2,[12] NiO,[13] Fe_2O_3,[14] and Nb_2O_5;[15] conducting polymers,[16,17] for example, polyaniline, polypyrrole, and polythiophene; and $Ni(OH)_2$ nanoparticles[18,19] have been used in pseudocapacitors because of their superior energy density, fast redox behavior, high specific capacitance, and environment-friendly nature. Ternary metal oxides having formula $A_XB_{3−X}O_4$, where A and B are transition metals with spinel structures, like $NiCo_2O_4$,[20,21] $CoFe_2O_4$,[22] $NiMn_2O_4$,[23] $MnCo_2O_4$,[24] $CuCo_2O_4$,[25] etc., have shown outstanding supercapacitive performance and excellent stability during cycling compared to their respective metal oxides mainly due to their superior electronic conductivity.[26]

Recently, layered double hydroxide (LDHs) materials have gained popularity as favorable electrode materials for super-capacitors owing to their high capacitance, distinctive structural properties having high surface area, fast redox reaction during charging and discharging, flexible ion

exchangeability, environment-friendly nature, and cost-effective scalability.[27] LDHs are originally inorganic claylike materials having two-dimensional morphology with highly tunable hydrotalcite-like layered structure.[28] LDHs contain positively charged metal hydroxide layers and weakly bonded charge-balancing anions and intercalating water molecules.[29] These are represented by the general formula $[M_{(1-X)}^{2+}M_{(X)}^{3+}(OH)_2]^{X+}[A^{n-}]_{X/n} \cdot mH_2O$, where M^{2+} and M^{3+} are the divalent (i.e., Mg^{2+}, Ni^{2+}, Co^{2+}, Zn^{2+}) and trivalent (i.e., Fe^{3+}, Al^{3+}, Mn^{3+}) metal cations and A^{n-} are the anions, i.e., OH^-, SO_4^{2-}, CO_3^{2-}, NO_3^-, Cl^-, or F^-. In LDHs, water molecules are hosted in between the cationic layers as neutral molecule and hydrogen-bonded with cationic layers.[30,31] The value of X in LDHs crystal structure generally varies from 0.25 to 0.33, providing the composition tunability of LDHs.[32]

It is worth noting from the literature that LDH materials have been considered as supercapacitive materials due to their resemblance of charge-storing mechanism and high power density. Brousse and co-workers showed that their charge–discharge and cyclic voltammetry (CV) profiles are different from those of pure pseudocapacitive materials, i.e., MnO_2, RuO_2.[33−35] Thus, LDH materials should be considered as battery-like materials. NiCo LDHs have attracted significant attention because of good performance as an electrode material (790 C g^{-1} at 2 A g^{-1}).[36] Chen and co-authors reported a specific capacitance of 2498 F g^{-1} at 1 A g^{-1} current density for nitrogen-doped mesoporous carbon/NiCo LDHs composite.[37] Wang et al. achieved a specific capacitance of 2762 F g^{-1} (1243 C g^{-1}) at a current density of 1 A g^{-1}.[38] CoAl LDH/graphene composites have achieved a specific capacitance of 479 F g^{-1} at a current density of 1 A g^{-1}.[39] Bai et al. reported carbon nanotube/NiAl LDH composites and showed a specific capacitance of 694 F g^{-1} at a current density of 1 A g^{-1}.[40] Atomically thin NiFe LDH three-dimensional (3D) microspheres showed a specific capacitance of 1061 F g^{-1} at a current density of 1 A g^{-1}.[41] Lv et al. reported glucose-interclated NiMn LDH materials and showed a specific capacitance of 1464 F g^{-1} at a current density of 0.5 A g^{-1}, whereas pristine NiMn LDH showed only 852 F g^{-1}.[42] MgAl LDH/reduced graphene oxide nanocomposite showed a specific capacitance of 1334 F g^{-1} at a current density of 1 A g^{-1}.[43] To the best of our knowledge, there is no study available over hydrothermally tailored nickel–vanadium layered double hydroxide (NiV LDHs) materials for supercapcitor application.

Herein, we report the syntheis of NiV LDH nanosheets having various compositions based on the amount of Ni and V ($Ni_{0.67}V_{0.33}$ LDH, $Ni_{0.75}V_{0.25}$ LDH, and $Ni_{0.80}V_{0.20}$ LDH) using a simple, low-cost, and potentially scalable hydrothermal technique. The as-prepared NiV LDH nanosheets were coated on Ni foam and used as supercapacitor electrode. Scanning electron microscopy (SEM), transmission electron microscopy (TEM), X-ray diffraction (XRD), Brunauer–Emmett–Teller (BET), and X-ray photoelectron spectroscopy (XPS) techniques were used for their morphological, structural, and physical characterizations, while electrochemical characterization techniques such as CV, galvanostatic charge–discharge (GCD), and electrochemical impedance spectroscopy (EIS) were used to study the electrochemical properties of NiV LDH nanosheets. Electrochemical characterizations of NiV LDH nanosheets display outstanding pseudocapacitance performance for $Ni_{0.80}V_{0.20}$ LDH. A high specific capacity of 711 C g^{-1} (1581 F g^{-1}) was achieved at a current density of 1 A g^{-1}, which remained 549 C g^{-1} (1220 F g^{-1}) at a higher current

density of 10 A g^{-1}. Moreover, a hybrid supercapacitor (HSC) device with a working potential of 1.5 V was fabricated using $Ni_{0.80}V_{0.20}$ LDH as positive electrode and commercial activated carbon as negative electrode. The HSC device exhibited a higher energy density of 30.6 Wh kg^{-1} at a power density of 0.78 kW kg^{-1}, which remained at 24 Wh kg^{-1} at a high power density of 11.1 kW kg^{-1}. This work suggests that the $Ni_{0.80}V_{0.20}$ LDH material can be an excellent candidate for improving the energy density of the HSC device.

2. RESULTS AND DISCUSSION

2.1. Structural and Morphological Characterization.
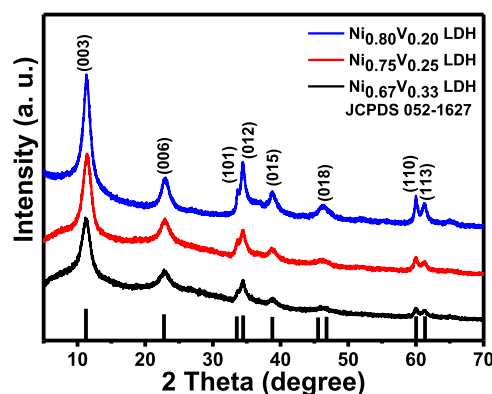Figure 1 shows typical XRD patterns of $Ni_{0.67}V_{0.33}$ LDH,

Figure 1. XRD patterns of $Ni_{0.67}V_{0.33}$ LDH, $Ni_{0.75}V_{0.25}$ LDH, and $Ni_{0.80}V_{0.20}$ LDH.

$Ni_{0.75}V_{0.25}$ LDH, and $Ni_{0.80}V_{0.20}$ LDH. The XRD spectra of $Ni_{0.67}V_{0.33}$ LDH, $Ni_{0.75}V_{0.25}$ LDH, and $Ni_{0.80}V_{0.20}$ LDH matched well with the standard nickel–vanadium carbonate hydroxide hydrate (JCPDS 052-1627). The characteristic peaks of the as-synthesized NiV LDHs at 11.25, 22.78, 33.54, 34.47, 38.78, 45.55, 46.79, 60.03, and 61.34° with respect to their corresponding (hkl) planes of (003), (006), (101), (012), (015), (018), (0012), (110), and (113) indicate the LDH formation during the hydrothermal synthesis (Scheme 1). It can be noted that there was no peak appearance for impurities found in the recorded spectra. Crystallinity of $Ni_{0.80}V_{0.20}$ LDH was higher compared to $Ni_{0.67}V_{0.33}$ LDH and $Ni_{0.75}V_{0.25}$ LDH (Table S1).[44] In addition, the interlayer distances for the d_{003} plane calculated form Bragg's formula were found to be approximately 0.77, 0.78, and 0.79 nm in $Ni_{0.67}V_{0.33}$ LDH, $Ni_{0.75}V_{0.25}$ LDH, and $Ni_{0.80}V_{0.20}$ LDH, respectively.[45] Literature studies suggest that α phase of LDHs have larger interlayer spacing than β phase of LDHs (0.46 nm), which was used to store more neutral water molecules and carbonate anions at the interlayers.[46] Thus, theoretically, α phase LDHs can be more electrochemically active than β phase LDHs.[47,48] The XRD spectra for pure Ni hydroxide and V-based hydroxide are given in Figure S1, which shows that the XRD spectra of the former matched nicely with pure hexagonal α-$Ni(OH)_2$ (JCPDS file 38-0715). However, different characteristics are observed for the latter due to its low crystallinity. Surface morphologies of $Ni_{0.67}V_{0.33}$ LDH, $Ni_{0.75}V_{0.25}$ LDH, and $Ni_{0.80}V_{0.20}$ LDH were investigated by field emission SEM (FESEM) images. Figure 2a–f shows three-dimensional morphology composed of curved nanosheets for all NiV LDHs.[41] The morphologies of Ni hydroxide and V-based hydroxides are shown in Figure S2. To understand the

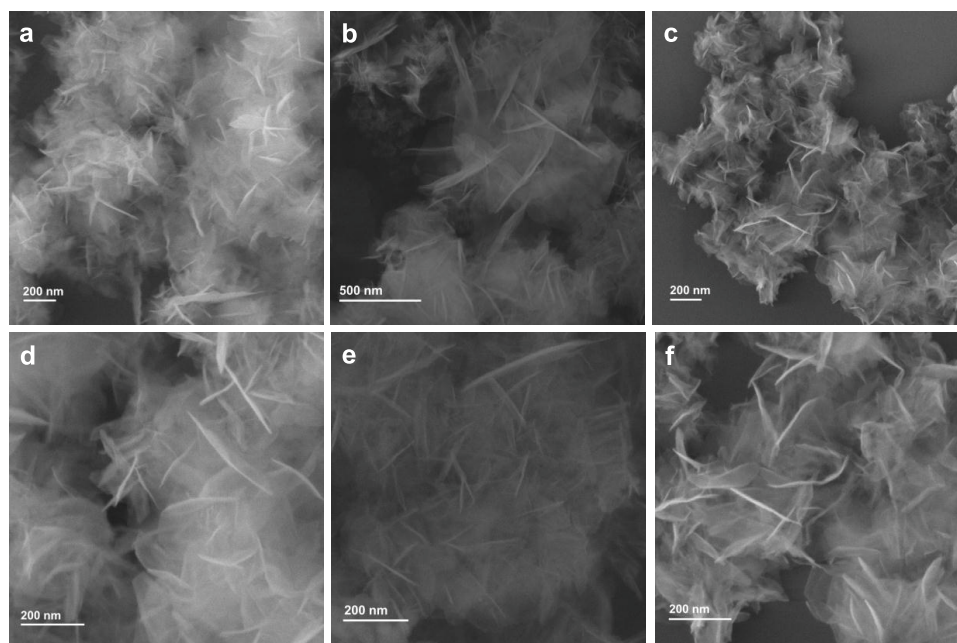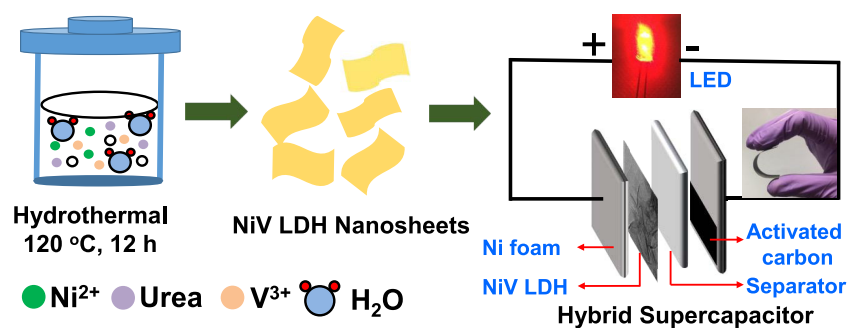**Scheme 1. Synthesis of NiV LDH and Fabrication of HSC**

Figure 2. ((a, d), (b, e), and (c, f)) Low- and high-magnification FESEM images of $Ni_{0.67}V_{0.33}$ LDH, $Ni_{0.75}V_{0.25}$ LDH, and $Ni_{0.80}V_{0.20}$ LDH, respectively.
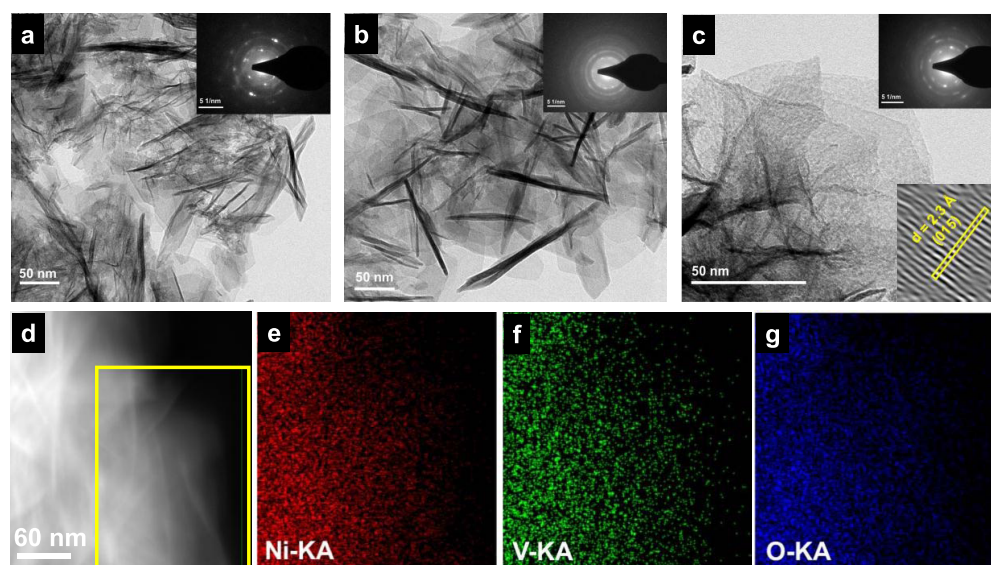

Figure 3. (a−c) TEM images of $Ni_{0.67}V_{0.33}$ LDH, $Ni_{0.75}V_{0.25}$ LDH, and $Ni_{0.80}V_{0.20}$ LDH, respectively, and the insets show their corresponding SAED patterns, as well as the HRTEM image of $Ni_{0.80}V_{0.20}$ LDH. (d) TEM image of $Ni_{0.80}V_{0.20}$ LDH. (e−g) Elemental mapping for Ni, V, and O corresponding to the area selected in (d).
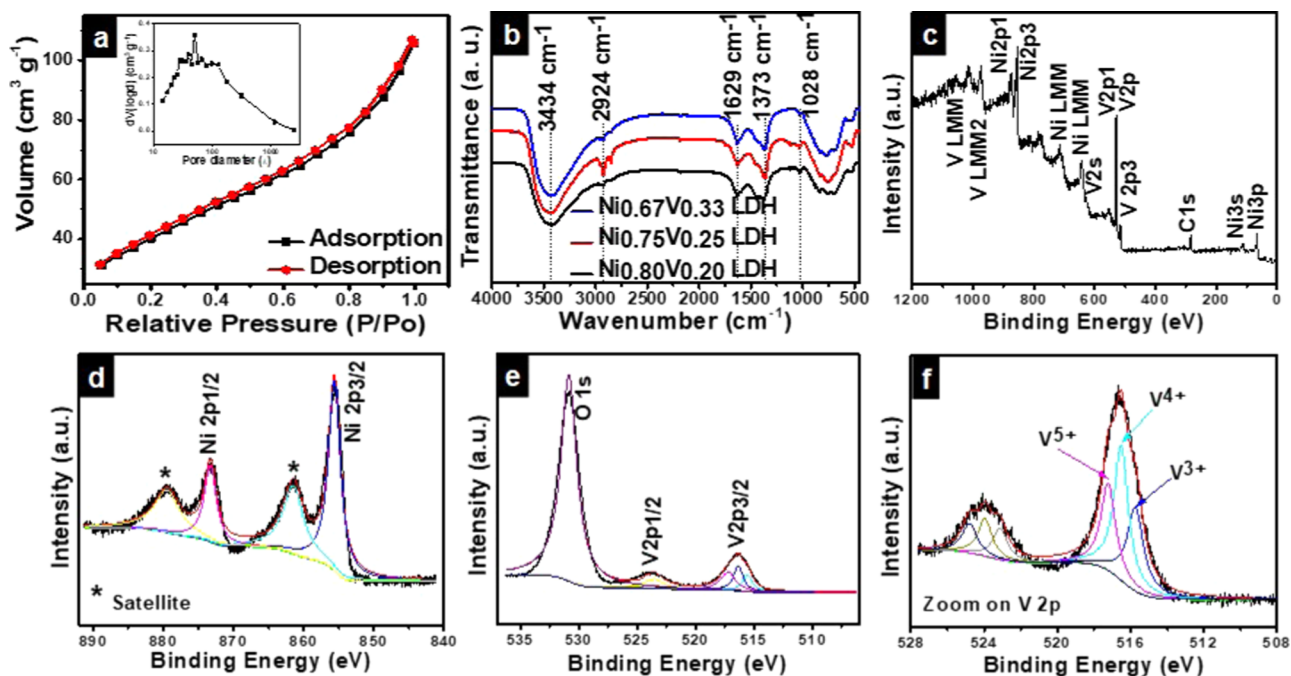
Figure 4. (a) Nitrogen adsorption−desorption isotherm of $Ni_{0.80}V_{0.20}$ LDH; the inset of (a) shows the BJH pore size distribution of $Ni_{0.80}V_{0.20}$ LDH. (b) FTIR curves for $Ni_{0.67}V_{0.33}$ LDH, $Ni_{0.75}V_{0.25}$ LDH, and $Ni_{0.80}V_{0.20}$ LDH;. (c) XPS survey scan for various elements for $Ni_{0.80}V_{0.20}$ LDH. (d) Ni 2p core-level spectra for $Ni_{0.80}V_{0.20}$ LDH. (e) O 1s and V 2p core-level spectra for $Ni_{0.80}V_{0.20}$ LDH. (f) Zoom on V 2p core-level spectra for $Ni_{0.80}V_{0.20}$ LDH.

layer stacking and its respective morphology of the as-synthesized NiV LDHs, TEM studies were carried out. Figure 3a−c shows the TEM images of $Ni_{0.67}V_{0.33}$ LDH, $Ni_{0.75}V_{0.25}$ LDH, and $Ni_{0.80}V_{0.20}$ LDH, respectively. The TEM images confirm that the nanosheets' thickness decreases as the amount of Ni content is increased in the NiV LDHs, and it is observed that 1−2 nm thick nanosheets were formed for $Ni_{0.80}V_{0.20}$ LDH. Selected area electron diffraction (SAED) patterns (inset of Figure 3a−c) confirm the polycrystalline behavior of all NiV LDH materials. Figures 3d−g and S3 confirm the uniform distribution of Ni, V, and O in the nanosheets of $Ni_{0.80}V_{0.20}$ LDH. The inset of Figure 3c shows the high-resolution TEM (HRTEM) image of $Ni_{0.80}V_{0.20}$ LDH, having the d-spacing of crystal lattice fringes to be 0.23 nm, which is assigned to the (015) plane of NiV LDH. This was consistent with the XRD result.[49] Figure 4a shows the nitrogen adsorption−desorption isotherm for $Ni_{0.80}V_{0.20}$ LDH. Nitrogen adsorption−desorption isotherms for $Ni_{0.67}V_{0.33}$ LDH and $Ni_{0.75}V_{0.25}$ LDH are presented in Figure S4. The shape of the nitrogen adsorption−desorption curve was found to be type III isotherm with H1 hysteresis loop for all NiV LDH materials, confirming their mesoporous nature. The BET surface areas was found to be 111, 144, and 266 m² g⁻¹ for $Ni_{0.67}V_{0.33}$ LDH, $Ni_{0.75}V_{0.25}$ LDH, and $Ni_{0.80}V_{0.20}$ LDH materials, respectively. The Barrett−Joyner−Halenda (BJH) pore size distribution curve in the inset of Figure 4a shows that pores are in the size range of 1−10 nm for all LDH materials, along with pore volumes of 0.140, 0.155, and 0.336 cm³ g⁻¹ for $Ni_{0.67}V_{0.33}$ LDH, $Ni_{0.75}V_{0.25}$ LDH, and $Ni_{0.80}V_{0.20}$ LDH, respectively. Most of the pores lie in the mesoporous range of 2−50 nm, thereby enhancing the electrochemical performance of the NiV LDHs.[50] The BET surface area is higher for $Ni_{0.80}V_{0.20}$ LDH due to its more exfoliated morphology compared to $Ni_{0.67}V_{0.33}$ LDH and $Ni_{0.75}V_{0.25}$ LDH, as supported by FESEM studies. Fourier transform infrared (FTIR) analysis was carried out to

know the bonding between the interlayers of LDHs. The FTIR spectra of $Ni_{0.67}V_{0.33}$ LDH, $Ni_{0.75}V_{0.25}$ LDH, and $Ni_{0.80}V_{0.20}$ LDH are shown in Figure 4b. The broad and strong absorption bands in Figure 4b at 3434 and 1629 cm⁻¹ indicate the presence of stretching and bending modes of hydroxyl groups, arising from interlayer water molecules and metal-hydroxyl groups.[51] Interlayer anion CO_3^{2-} was confirmed through the presence of a vibration band at ∼1373 cm⁻¹. The band at 2924 cm⁻¹ was assigned to the $CO_3^{2-}-H_2O$ stretching vibration, confirming the presence of hydrogen-bonded water molecules with carbonate anions in the interlayers of NiV LDHs.[52] A shoulder band at ∼1028 cm⁻¹ confirms the vibration band of hydroxyl groups, which are mainly corresponding to metal cations (Ni^{2+} and V^{3+}). Bands at lower wavenumbers (less than 800 cm⁻¹) were noted due to the stretching vibrations of metal−oxygen bonds present in NiV LDHs.[53,54] Figure 4c−f shows the XPS survey scan and the corresponding core-level spectra of $Ni_{0.80}V_{0.20}$ LDH. In this figure, two peaks at ∼855.6 and ∼873.3 eV correspond to Ni $2p_{3/2}$ and Ni $2p_{1/2}$, respectively, and are found along with two satellite peaks at ∼861.6 and ∼879.5 eV, indicating the native characteristic of Ni^{2+} spectra.[55,56] The difference between the binding energies of the Ni $2p_{3/2}$ and Ni $2p_{1/2}$ peaks was found to be ∼17.7 eV.[57,58] Figure 4e shows the O 1s and V 2p spectra, which confirm the O 1s core-level peak at ∼530.9 eV. The V 2p spectrum also confirms the presence of V $2p_{1/2}$ and V $2p_{3/2}$ peaks due to the spinning p orbital splitting. The difference between the binding energies of V $2p_{1/2}$ and V $2p_{3/2}$ is found to be ∼7.5 eV.[59] V $2p_{3/2}$ spectrum in Figure 4f can be deconvoluted into three peaks, corresponding to V (III) (∼515.7 eV), V (IV) (∼516.5 eV), and V (V) (∼517.2 eV). This confirms that V is partially oxidized to +4 and +5 oxidation states during hydrothermal treatment.[60,61] A similar behavior was evidenced from the XPS images of $Ni_{0.67}V_{0.33}$ LDH and $Ni_{0.75}V_{0.25}$ LDH (Figures S5 and S6).

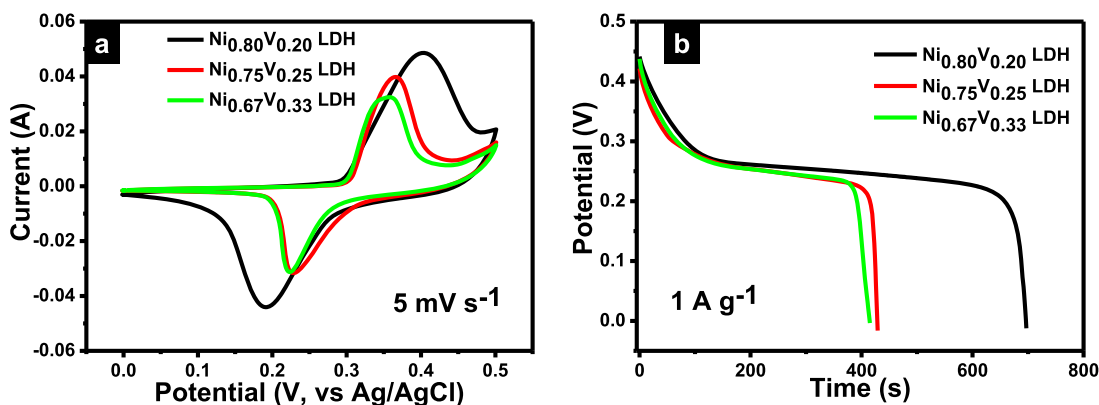**Figure 5.** (a) Comparison of CV curves at 5 mV s^{-1} scan rate for Ni$_{0.67}$V$_{0.33}$ LDH, Ni$_{0.75}$V$_{0.25}$ LDH, and Ni$_{0.80}$V$_{0.20}$ LDH. (b) Comparison of GCD curves at 1 A g^{-1} current density for Ni$_{0.67}$V$_{0.33}$ LDH, Ni$_{0.75}$V$_{0.25}$ LDH, and Ni$_{0.80}$V$_{0.20}$ LDH.
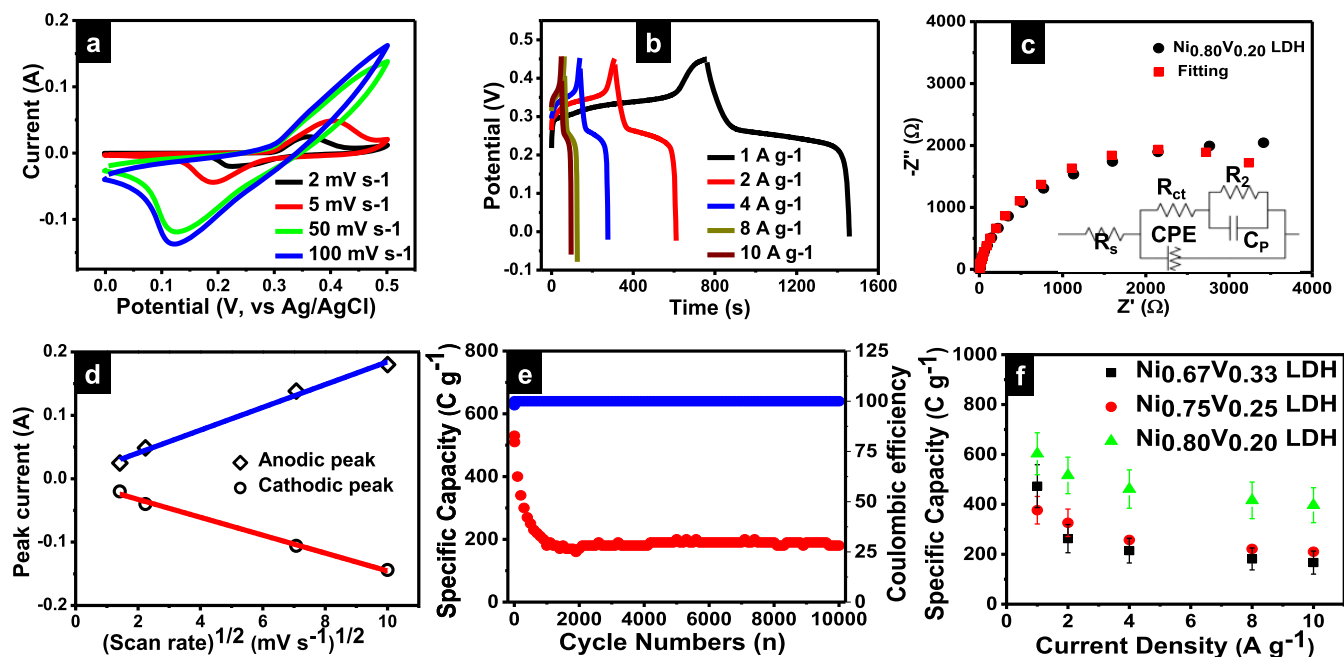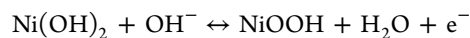

Figure 6. (a) CV curves for Ni$_{0.80}$V$_{0.20}$ LDH at various scan rates. (b) GCD curves for Ni$_{0.80}$V$_{0.20}$ LDH at various current densities. (c) EIS curve for Ni$_{0.80}$V$_{0.20}$ LDH. (d) Peak current verses scan rate for Ni$_{0.80}$V$_{0.20}$ LDH. (e) Specific capacity retention and Coulombic efficiency with number of cycles for Ni$_{0.80}$V$_{0.20}$ LDH. (f) Specific capacity variation with current density for Ni$_{0.67}$V$_{0.33}$ LDH, Ni$_{0.75}$V$_{0.25}$ LDH, and Ni$_{0.80}$V$_{0.20}$ LDH.

3. ELECTROCHEMICAL CHARACTERIZATION

3.1. Three-Electrode Testing. A three-electrode set up was used to investigate the electrochemical performance of as-synthesized Ni$_{0.67}$V$_{0.33}$ LDH, Ni$_{0.75}$V$_{0.25}$ LDH, and Ni$_{0.80}$V$_{0.20}$ LDH. CV studies were carried out for the potential window of 0−0.5 V in the presence of 2 M KOH aqueous electrolyte. Figure 5a shows the comparison of CV curves at 5 mV s^{-1} scan rate for Ni$_{0.67}$V$_{0.33}$ LDH, Ni$_{0.75}$V$_{0.25}$ LDH, and Ni$_{0.80}$V$_{0.20}$ LDH, respectively. From the CV curves in Figure 5a, it can be inferred that composition of NiV LDHs influences redox peak position as the peak shifts toward positive voltage while varying the compositions of Ni and V from 2:1 to 4:1. In addition, CV curves show a couple of distinct redox peaks for all NiV LDHs. At the same time, it was proved from galvanostatic discharge curves in Figure 5b that appearance of nonlinear shape for all of the NiV LDHs exemplifies the quasi-reversible electron transfer between electrode material and electrolyte ions, which further confirms that the measured specific capacitances arise through redox mechanism.[37,62] Evidently, the integral area

under the CV curve of Ni$_{0.80}$V$_{0.20}$ LDH was comparatively larger than that for Ni$_{0.67}$V$_{0.33}$ LDH and Ni$_{0.75}$V$_{0.25}$ LDH, revealing its better supercapacitive performance. Supporting the previous claim, the longer discharge time for Ni$_{0.80}$V$_{0.20}$ LDH compared to Ni$_{0.67}$V$_{0.33}$ LDH and Ni$_{0.75}$V$_{0.25}$ LDH also infers its better supercapacitive performance. In addition, the characteristics of the CV curve for Ni$_{0.80}$V$_{0.20}$ LDH did not change much even after the scan rate was increased from 2 to 100 mV s^{-1} (Figure 6a). The CV curve suggests that redox current increases as the scan rate increases. Also, as the scan rate is increased, the anodic and cathodic peaks of LDH shift further toward positive and negative sides, respectively, indicating the reversible Faradic process. The redox peaks in the CV curves were due to the surface redox reaction of Ni^{2+} and NiOOH, present in NiV LDH.[63,64]

$$Ni(OH)_2 + OH^- \leftrightarrow NiOOH + H_2O + e^-$$

GCD curves for Ni$_{0.80}$V$_{0.20}$ LDH show that the shape of the charge−discharge curve was retained as the current density was
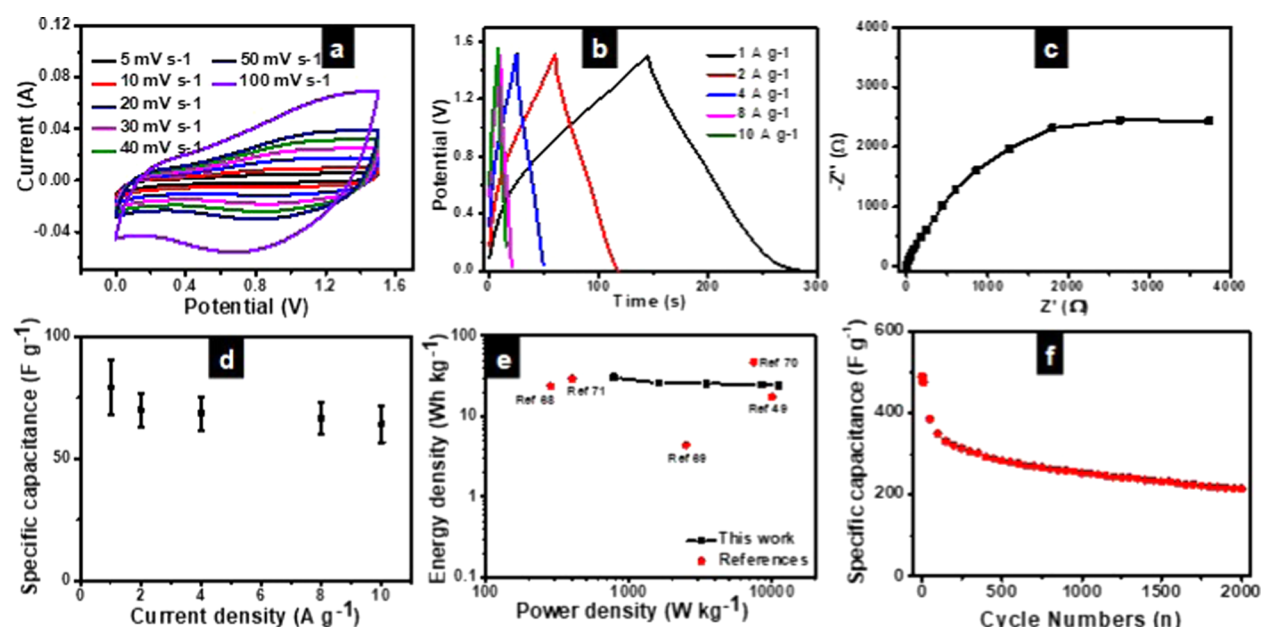
Figure 7. (a) CV curves for HSC at various scan rates. (b) GCD curves for HSC at various current densities. (c) EIS curve for HSC. (d) Specific capacitance variation with current density for HSC. (e) Ragone plot for HSC. (f) Retention of specific capacitance with number of cycles at current density of 1 A g^{-1} for HSC.

changed from 1 to 10 A g^{-1}, confirming the high rate capability of NiV LDH material. The shape of the GCD curves also confirms the battery-like behavior of NiV LDH material.[65] The maximum specific capacities of Ni$_{0.80}$V$_{0.20}$ LDH were found to be 711 C g^{-1} (1581 F g^{-1}), 622 C g^{-1} (1382 F g^{-1}), 580 C g^{-1} (1289 F g^{-1}), 559 C g^{-1} (1242 F g^{-1}), and 549 C g^{-1} (1220 F g^{-1}) at current densities of 1, 2, 4, 8, and 10 A g^{-1}, respectively. Figure 6f shows the comparison of specific capacity retention and current density for Ni$_{0.67}$V$_{0.33}$ LDH, Ni$_{0.75}$V$_{0.25}$ LDH, and Ni$_{0.80}$V$_{0.20}$ LDH using specific capacitance data for three different electrodes for each NiV LDH material. The rate capability of Ni$_{0.80}$V$_{0.20}$ LDH (~77%), as calculated from the GCD curves, was higher compared to Ni$_{0.67}$V$_{0.33}$ LDH (~58%) and Ni$_{0.75}$V$_{0.25}$ LDH (~35.5%) as the current density was increased from 1 to 10 A g^{-1}. The CV and GCD curves for Ni$_{0.67}$V$_{0.33}$ LDH and Ni$_{0.75}$V$_{0.25}$ LDH are shown in Figure S7. Figures S8 and S9 show the electrochemical characterization for pure Ni hydroxide and V hydroxides, respectively, suggesting that Ni hydroxide has better redox behavior than V-based hydroxides. Figure S10 presents the comparison of CV curves for Ni foam, V-based hydroxide, Ni hydroxide, and Ni$_{0.80}$V$_{0.20}$ LDH at a scan rate of 5 mV s^{-1}. The CV curves show that contribution of Ni foam is negligible and area under the curve is maximum for Ni$_{0.80}$V$_{0.20}$ LDH. Table S3 exhibits comparative specific capacitances for the electrodes with active materials of pure Ni hydroxide, V hydroxide, Ni$_{0.67}$V$_{0.33}$ LDH, Ni$_{0.75}$V$_{0.25}$ LDH, and Ni$_{0.80}$V$_{0.20}$ LDH at different current densities, showing that Ni$_{0.80}$V$_{0.20}$ LDHs have higher specific capacitance. The average specific capacities (average of three electrodes) of pure Ni hydroxide, V hydroxide, Ni$_{0.67}$V$_{0.33}$ LDH, Ni$_{0.75}$V$_{0.25}$ LDH, and Ni$_{0.80}$V$_{0.20}$ LDH were found to be 197 C g^{-1} (467 F g^{-1}), 60 C g^{-1} (144 F g^{-1}), 377 C g^{-1} (839 F g^{-1}), 473 C g^{-1} (1104 F g^{-1}), and 603 C g^{-1} (1366 F g^{-1}), respectively, at a current density of 1 A g^{-1}. The EIS images of Ni$_{0.67}$V$_{0.33}$ LDH, Ni$_{0.75}$V$_{0.25}$ LDH, and Ni$_{0.80}$V$_{0.20}$ LDH shown in Figure S11 reveal the higher specific capacitance for Ni$_{0.80}$V$_{0.20}$ LDH compared to Ni$_{0.67}$V$_{0.33}$ LDH

and Ni$_{0.75}$V$_{0.25}$ LDH. It further infers that experimental data points well corroborated with the fitted data points (Figure 6c). The overall resistance, i.e., combining electrolyte (R_s) and contact resistances, and resistance due to electroactive material, was found to be 4.54 kΩ for Ni$_{0.80}$V$_{0.20}$ LDH. In addition, the charge-transfer resistance (R_{ct}) for Ni$_{0.80}$V$_{0.20}$ LDH was found to be 883 mΩ (Table S2). Hence, it can be inferred that the better supercapacitive performance of Ni$_{0.80}$V$_{0.20}$ LDH was due to its more exfoliated morphology across the layers, which helps in channelizing more electrolyte ions interaction with the electrode active surface and thus results in more redox reaction.[66] The linear relationship between the peak current for anodic and cathodic peaks vs square root of scan rate, as shown in Figure 6d, confirms bulk intercalation of electrolyte ions into the surface of Ni$_{0.80}$V$_{0.20}$ LDH, which facilitates bulk redox reaction.[26] Figure 6e presents the specific capacitance retention of Ni$_{0.80}$V$_{0.20}$ LDH with the number of cycles at a current density of 1 A g^{-1}. It is noted from the cycling curves that the specific capacitance decreased up to 40% during the first 1000 cycles and then remained stable up to the next 10 000 cycles. So, the initial capacitance decay is attributed to structure collapse, phase transformation, and reduction in active surface area.[67] Columbic efficiency was found to be 100% up to 10 000 cycles.

3.2. Hybrid Supercapacitor Testing. To further assess the electrochemical performance of NiV LDH material, an HSC device was fabricated using Ni$_{0.80}$V$_{0.20}$ LDH as positive electrode and commercial activated carbon as negative electrode. Ni$_{0.80}$V$_{0.20}$ LDH was chosen due to its better supercapacitive performance in a three-electrode cell test, compared to other counterparts. Scheme 1 shows the fabrication of HSC device. Electrochemical results for commercial activated carbon are shown in Figure S12. Based on the GCD curves of activated carbon (Figure S12b) and Ni$_{0.80}$V$_{0.20}$ LDH (Figure 6b) at a current density of 1 A g^{-1}, the values of average specific capacitance were found to be 205 F g^{-1} (C_-) and 1366 F g^{-1} (C_+). The potential windows ΔV_+

Table 1. Comparison of Energy Density and Power Density with Other Materials

material	electrolyte	energy density (Wh kg^{-1})	power density (W kg^{-1})	ref
Ni(OH)$_2$/graphene	6 M KOH	36.7	~100	74
		~10.0	7980	
carbon/CoO nanoparticles	2 M KOH	25.0	350	75
		17.4	7000	
NiCo$_2$S$_4$/bio-carbon	2 M KOH	27.7	~264	76
		16.1	5000	
NiCo$_2$O$_4$@NiCo$_2$S$_4$/Ni foam	3 M KOH	35.6	1500	77
		14.4	7500	
NiO−CuO mesoporous nanowires	3 M KOH	33.8	400	78
		18.4	8000	
Co$_3$O$_4$/N-doped carbon hollow spheres	2 M KOH	34.5	753	79
		29.0	3807	
CoS hollow structures	2 M KOH	39.9	756	80
		~20.0	10 000	
Ni$_{0.80}$V$_{0.20}$ LDH	2 M KOH	30.6	780	this work
		24.6	11 100	

and ΔV_- are 0.45 and −1 V, respectively. According to eq 1, the optimum ratio of m_- and m_+ was found to be 2.78. The CV curves of Ni$_{0.80}$V$_{0.20}$ LDH and commercial activated carbon were measured using a three-electrode system at a scan rate of 50 mV s^{-1} in 2 M KOH electrolyte and are plotted in Figure S13, which suggests the optimized operating potential window for HSC to be 1.5 V. Figure 7a presents the CV curves of Ni$_{0.80}$V$_{0.20}$ LDH/activated carbon HSC at different scan rates from 5 to 100 mV s^{-1}. The shape of the CV curves is almost rectangular with small redox peaks present in the anodic and cathodic parts of the curves, suggesting the pseudocapacitive behavior of HSC. There was no obvious distortion in the shape of CV curve even at different scan rates from 5 to 100 mV s^{-1}, thus confirming the higher rate capability and fast charge−discharge properties of HSC.[50] The GCD curves for Ni$_{0.80}$V$_{0.20}$ LDH/activated carbon HSC are shown in Figure 7b. The shape of the GCD curves is triangular with small deviation in linear shape, confirming the pseudocapacitive charge storage of Ni$_{0.80}$V$_{0.20}$ LDH/activated carbon HSC. The shape of the GCD curves remained same even at higher current densities of 1−10 A g^{-1}, suggesting the higher degree of electrochemical reversibility of redox process and good Columbic efficiency.[37,51] The maximum specific capacitance values for the constructed HSC device were found to be 98, 83, 82, 79, and 77 F g^{-1} at current densities of 1, 2, 4, 8, and 10 A g^{-1}, respectively. The variation of average specific capacitance of six such devices with current densities is shown in Figure 7d, confirming ~79% retention in average specific capacitance at a higher current density of 10 A g^{-1}. Ni$_{0.80}$V$_{0.20}$ LDH/activated carbon HSC device in Figure 7b shows a potential drop of 12 mV at 1 A g^{-1} current density, which was increased to 440 mV at 10 A g^{-1} current density. The EIS curve of Ni$_{0.80}$V$_{0.20}$ LDH/activated carbon HSC device in Figure 7c shows a similar shape to NiV LDH. The Ragone plot for Ni$_{0.80}$V$_{0.20}$ LDH/activated carbon HSC device is shown in Figure 7e. The device showed an excellent energy density of 30.6 Wh kg^{-1} at a power density of 0.78 kW kg^{-1}, which remained at 24 Wh kg^{-1} at a higher power density of 11.1 kW kg^{-1}. A comparison of energy density and power density with other reported materials is reported in Table 1. The cycling stability of Ni$_{0.80}$V$_{0.20}$ LDH/activated carbon HSC device is shown in Figure 7f.[51,68−71] The cycling study shows a rapid decrease in the specific capacitance for the first few ten cycles and then remained constant almost

up to 2000 cycles. The specific capacitance was found to be ~42% of the initial value after 2000 cycles. Moreover, Ni$_{0.80}$V$_{0.20}$ LDH/activated carbon HSC solid-state device with LiCl/poly(vinyl alcohol) gel electrolyte was successfully used to power a red light-emitting diode of 1.8 V for almost 2 min after charging with 8 mA.

4. CONCLUSIONS

In summary, we have successfully demonstrated a facile and cost-effective hydrothermal method for the synthesis of NiV LDH having controlled composition. Electrochemical studies showed that Ni$_{0.80}$V$_{0.20}$ LDH shows better supercapacitive behavior than Ni$_{0.67}$V$_{0.33}$ LDH and Ni$_{0.75}$V$_{0.25}$ LDH due to its 3D exfoliated morphology. Ni$_{0.80}$V$_{0.20}$ LDH showed a maximum specific capacity of 711 C g^{-1} (1581 F g^{-1}) at a current density of 1 A g^{-1}, which remained at 549 C g^{-1} (1220 F g^{-1}) at a higher current density of 10 A g^{-1}. The HSC device based on Ni$_{0.80}$V$_{0.20}$ LDH/activated carbon showed a maximum specific capacitance of 98 F g^{-1} at a current density of 1 A g^{-1} with retention of ~79% (77 F g^{-1}) at a current density of 10 A g^{-1}. The energy density was found to be 30.6 Wh kg^{-1} at a power density of 0.78 kW kg^{-1}, which remained at 24 Wh kg^{-1} at a high power density of 11.1 kW kg^{-1}. These results suggest that NiV LDH nanostructures have significant potential as low-cost electrode material for the energy-storage devices.

5. EXPERIMENTAL SECTION

5.1. Materials. Nickel chloride (NiCl$_2$) (98%), vanadium chloride (VCl$_3$) (97%), potassium hydroxide (KOH), and poly(vinylidene fluoride) (PVDF, average MW = 534 000) were purchased from Sigma-Aldrich, India. Urea (99%), ethanol, N-methyl-2-pyrrolidone (NMP), and potassium hydroxide pellets were purchased from Merck, India. Conducting carbon black (Super P), activated carbon, and Ni foam were supplied from MTI Corporation.

5.2. Synthesis of NiV LDH Nanosheets. NiV LDH nanosheets were prepared through a one-step hydrothermal method. In a typical synthesis, various mole ratios of Ni/V (2:1, 3:1, and 4:1 for the synthesis of Ni$_{0.67}$V$_{0.33}$ LDH, Ni$_{0.75}$V$_{0.25}$ LDH, and Ni$_{0.80}$V$_{0.20}$ LDH, respectively) were taken in such a way that the amount of total ion concentration (Ni^{2+} and V^{3+}) remains 3.2 mmol. In brief, different ratios of NiCl$_2$

and VCl₃ and 0.3 g of urea were mixed in 40 mL of deionized (DI) water and stirred for 30 min to obtain a homogeneous solution. Then, the solution mixture was transferred to a Teflon-lined stainless steel autoclave and the reaction was performed at 120 °C for 12 h. After cooling down the autoclave to room temperature, the obtained powder was washed with DI water and ethanol. NiV LDH nanosheets were collected after drying the resultant powder at 60 °C in a vacuum oven overnight.[72] For comparison, pure Ni and V hydroxides were also prepared following the similar procedure.

5.3. Material Characterization. The surface morphologies of the as-synthesized LDHs were observed by field emission scanning electron microscopy (FESEM, Quanta 200, Zeiss, Germany). Transmission electron microscopy (FEI Titan G2 60-300 TEM (HRTEM)) was further used to observe the morphology, size, and composition of the as-synthesized LDHs. The crystal structures of various LDH materials were analyzed through X-ray diffraction (XRD) patterns obtained from an X-ray diffractometer (X'Pert Pro, PANanalytical, the Netherlands). Cu Kα (λ = 1.5406 Å) was used to obtain the XRD patterns. Fourier transform infrared (FTIR, PerkinElmer) spectroscopy using KBr pellet method was used to study the presence of functional groups in NiV LDHs. X-ray photoelectron spectroscopy (XPS) measurements were carried out using a PHI 5000 Versa Probe II, FEI Inc. spectrometer. XPS binding energy values for all of the samples were referenced to C 1s hydrocarbon peak at 284.6 eV. The Brunauer−Emmett−Teller (BET) surface area and Barrett−Joyner−Halenda (BJH) pore size distribution of the as-synthesized LDHs were measured through the N₂ adsorption−desorption method (Quantachrome Instruments).

5.4. Electrochemical Characterization. NiV LDH, PVDF, and super P were mixed in a weight ratio of 75:15:10 in NMP solvent to make a homogeneous slurry. Ni foam (1 cm × 3 cm) pieces were coated on a 1 cm × 1 cm area using this slurry and dried at 80 °C for 12 h to make the working electrodes. Pure Ni and pure V hydroxide electrodes were also prepared following the similar procedure. The material loading was kept in the range of 2−3 mg for all electrodes. A three-electrode electrochemical set up was used to study the supercapacitive performance of NiV LDH material. The three-electrode assembly consists of NiV LDH-coated Ni foam as the working electrode, Ag/AgCl/KCl, Pt rod as the reference electrode and counter electrode, and 2 M KOH as the electrolyte, respectively.

HSC devices were fabricated using NiV LDH materials and activated carbon as positive and negative electrodes, respectively. To maintain the charge on positive (q_+) and negative (q_-) electrodes, i.e., $q_+ \approx q_-$, the ratio of positive (m_+) to negative (m_-) electrodes was maintained according to the following equation

$$\frac{m_-}{m_+} = \frac{C_+ \times \Delta V_+}{C_- \times \Delta V_-} \tag{1}$$

where C_+ and C_- are the specific capacitances of positive and negative electrodes, respectively, and ΔV_+ and ΔV_- are the potential windows for the GCD process of positive and negative electrodes, respectively.[26] The optimum ratio was found to be 2.78 based on the specific capacitance values for positive and negative electrodes at 1 A g^{-1}. The electrochemical performance of NiV LDH and HSC was studied using potentiostat/galvanostat (Autolab 302N, Metrohm, the

Netherlands). Galvanostatic charge−discharge (GCD), cyclic voltammetry (CV), and electrochemical impedance spectroscopy (EIS) studies were conducted at the open-circuit voltage over a frequency range of 0.01 Hz−100 kHz. The specific capacitance (C_s) of active material was calculated through GCD curves using the following equations[73]

$$C_s = \frac{I\Delta t}{m\Delta V} \text{(specific capacitance, F g}^{-1}) \tag{2}$$

$$C = \frac{I\Delta t}{m} \text{(specific capacity, C g}^{-1}) \tag{3}$$

$$C_s = \frac{I\Delta t}{M\Delta V} \text{(specific capacitance of HSC device, F g}^{-1}) \tag{4}$$

where I is the current (A), m is the mass of active material (g) in the three-electrode system, M is the total mass of active materials at positive and negative electrodes in HSC, Δt is the discharging time (s), and ΔV is the applied potential window (V). The energy density (E, Wh kg^{-1}) and power density (P, W kg^{-1}) of HSC were calculated using the following equations

$$E = \frac{1}{2}C_s V^2 \tag{5}$$

$$P = \frac{E}{\Delta t} \tag{6}$$

■ ASSOCIATED CONTENT

ⓢ Supporting Information

The Supporting Information is available free of charge on the ACS Publications website at DOI: 10.1021/acsomega.8b03618.

> XRD and FESEM for Ni and V hydroxide; BET and XPS data for Ni₀.₆₇V₀.₃₃ and Ni₀.₇₅V₀.₂₅ LDH; electrochemical data for Ni/V hydroxide and Ni₀.₆₇V₀.₃₃/Ni₀.₇₅V₀.₂₅ LDH; and EIS data for Ni₀.₆₇V₀.₃₃ LDH, Ni₀.₇₅V₀.₂₅ LDH and Ni₀.₈₀V₀.₂₀ LDH (PDF)

■ AUTHOR INFORMATION

Corresponding Author

*E-mail: guptark@iitk.ac.in. Tel: +91-5122596972. Fax: +91-5122590104.

ORCID Ⓘ

Vijay Kumar Thakur: 0000-0002-0790-2264

Raju Kumar Gupta: 0000-0002-5537-8057

Notes

The authors declare no competing financial interest.

■ ACKNOWLEDGMENTS

■ REFERENCES

(1) Conway, B. E. *Electrochemical Supercapacitors: Scientific Fundamentals and Technological Applications*; Springer, 2013.

(2) Simon, P.; Gogotsi, Y. Materials for electrochemical capacitors. *Nat. Mater.* **2008**, 7, 845−854.

(3) Wang, G.; Zhang, L.; Zhang, J. A review of electrode materials for electrochemical supercapacitors. *Chem. Soc. Rev.* **2012**, *41*, 797−828.

(4) Tyagi, A.; Tripathi, K. M.; Gupta, R. K. Recent progress in micro-scale energy storage devices and future aspects. *J. Mater. Chem. A* **2015**, *3*, 22507−22541.

(5) Winter, M.; Brodd, R. J. What are batteries, fuel cells, and supercapacitors? *Chem. Rev.* **2004**, *104*, 4245−4270.

(6) Kötz, R.; Carlen, M. Principles and applications of electrochemical capacitors. *Electrochim. Acta* **2000**, *45*, 2483−2498.

(7) Liu, C.; Li, F.; Ma, L.-P.; Cheng, H.-M. Advanced materials for energy storage. *Adv. Mater.* **2010**, *22*, E28−E62.

(8) Burke, A. Ultracapacitors: Why, how, and where is the technology. *J. Power Sources* **2000**, *91*, 37−50.

(9) Meher, S. K.; Rao, G. R. Ultralayered Co_3O_4 for high-performance supercapacitor applications. *J. Phys. Chem. C* **2011**, *115*, 15646−15654.

(10) Wei, W.; Cui, X.; Chen, W.; Ivey, D. G. Manganese oxide-based materials as electrochemical supercapacitor electrodes. *Chem. Soc. Rev.* **2011**, *40*, 1697−1721.

(11) Sugimoto, W.; Yokoshima, K.; Murakami, Y.; Takasu, Y. Charge storage mechanism of nanostructured anhydrous and hydrous ruthenium-based oxides. *Electrochim. Acta* **2006**, *52*, 1742−1748.

(12) Zhang, J.; Wang, Y.; Wu, J.; Shu, X.; Yu, C.; Cui, J.; Qin, Y.; Zhang, Y.; Ajayan, P. M.; Wu, Y. Remarkable supercapacitive performance of TiO_2 nanotube arrays by introduction of oxygen vacancies. *Chem. Eng. J.* **2017**, *313*, 1071−1081.

(13) Yang, Z.; Xu, F.; Zhang, W.; Mei, Z.; Pei, B.; Zhu, X. Controllable preparation of multishelled NiO hollow nanospheres via layer-by-layer self-assembly for supercapacitor application. *J. Power Sources* **2014**, *246*, 24−31.

(14) Zhang, M.; Sha, J.; Miao, X.; Liu, E.; Shi, C.; Li, J.; He, C.; Li, Q.; Zhao, N. Three-dimensional graphene anchored Fe_2O_3@C core-shell nanoparticles as supercapacitor electrodes. *J. Alloys Compd.* **2017**, *696*, 956−963.

(15) Kong, L.; Zhang, C.; Wang, J.; Qiao, W.; Ling, L.; Long, D. Nanoarchitectured Nb_2O_5 hollow, Nb_2O_5@carbon and NbO_2@carbon core-shell microspheres for ultrahigh-rate intercalation pseudocapacitors. *Sci. Rep.* **2016**, *6*, No. 21177.

(16) Shown, I.; Ganguly, A.; Chen, L.-C.; Chen, K.-H. Conducting polymer-based flexible supercapacitor. *Energy Sci. Eng.* **2015**, *3*, 2−26.

(17) Kim, J.; Lee, J.; You, J.; Park, M.-S.; Hossain, M. S. A.; Yamauchi, Y.; Kim, J. H. Conductive polymers for next-generation energy storage systems: Recent progress and new functions. *Mater. Horiz.* **2016**, *3*, 517−535.

(18) Wang, R.; Lang, J.; Liu, Y.; Lin, Z.; Yan, X. Ultra-small, size-controlled $Ni(OH)_2$ nanoparticles: Elucidating the relationship between particle size and electrochemical performance for advanced energy storage devices. *NPG Asia Mater.* **2015**, *7*, No. e183.

(19) Liu, Y.; Wang, R.; Yan, X. Synergistic effect between ultra-small nickel hydroxide nanoparticles and reduced graphene oxide sheets for the application in high-performance asymmetric supercapacitor. *Sci. Rep.* **2015**, *5*, No. 11095.

(20) Zhang, G.; Lou, X. W. General solution growth of mesoporous $NiCo_2O_4$ nanosheets on various conductive substrates as high-performance electrodes for supercapacitors. *Adv. Mater.* **2013**, *25*, 976−979.

(21) Zhang, G.; Lou, X. W. Controlled growth of $NiCo_2O_4$ nanorods and ultrathin nanosheets on carbon nanofibers for high-performance supercapacitors. *Sci. Rep.* **2013**, *3*, No. 1470.

(22) Wang, Z.; Jia, W.; Jiang, M.; Chen, C.; Li, Y. One-step accurate synthesis of shell controllable $CoFe_2O_4$ hollow microspheres as high-performance electrode materials in supercapacitor. *Nano Res.* **2016**, *9*, 2026−2033.

(23) Zhang, M.; Guo, S.; Zheng, L.; Zhang, G.; Hao, Z.; Kang, L.; Liu, Z.-H. Preparation of $NiMn_2O_4$ with large specific surface area from an epoxide-driven sol−gel process and its capacitance. *Electrochim. Acta* **2013**, *87*, 546−553.

(24) Tholkappiyan, R.; Naveen, A. N.; Sumithra, S.; Vishista, K. Investigation on spinel $MnCo_2O_4$ electrode material prepared via controlled and uncontrolled synthesis route for supercapacitor application. *J. Mater. Sci.* **2015**, *50*, 5833−5843.

(25) Jadhav, H. S.; Pawar, S. M.; Jadhav, A. H.; Thorat, G. M.; Seo, J. G. Hierarchical mesoporous 3D flower-like $CuCo_2O_4$/NF for high-performance electrochemical energy storage. *Sci. Rep.* **2016**, *6*, No. 31120.

(26) Chen, H.; Chang, X.; Chen, D.; Liu, J.; Liu, P.; Xue, Y.; Lin, H.; Han, S. Graphene-karst cave flower-like Ni−Mn layered double oxides nanoarrays with energy storage electrode. *Electrochim. Acta* **2016**, *220*, 36−46.

(27) Daud, M.; Kamal, M. S.; Shehzad, F.; Al-Harthi, M. A. Graphene/layered double hydroxides nanocomposites: A review of recent progress in synthesis and applications. *Carbon* **2016**, *104*, 241−252.

(28) Shao, M.; Zhang, R.; Li, Z.; Wei, M.; Evans, D. G.; Duan, X. Layered double hydroxides toward electrochemical energy storage and conversion: Design, synthesis and applications. *Chem. Commun.* **2015**, *51*, 15880−15893.

(29) Sarfraz, M.; Shakir, I. Recent advances in layered double hydroxides as electrode materials for high-performance electrochemical energy storage devices. *J. Energy Storage* **2017**, *13*, 103−122.

(30) ten Elshof, J. E.; Yuan, H.; Gonzalez Rodriguez, P. Two-dimensional metal oxide and metal hydroxide nanosheets: Synthesis, controlled assembly and applications in energy conversion and storage. *Adv. Energy Mater.* **2016**, *6*, No. 1600355.

(31) Wang, Q.; O'Hare, D. Recent advances in the synthesis and application of layered double hydroxide (LDH) nanosheets. *Chem. Rev.* **2012**, *112*, 4124−4155.

(32) Zhao, M.; Zhao, Q.; Li, B.; Xue, H.; Pang, H.; Chen, C. Recent progress in layered double hydroxide based materials for electrochemical capacitors: Design, synthesis and performance. *Nanoscale* **2017**, *9*, 15206−15225.

(33) Zhang, L.; Hui, K. N.; San Hui, K.; Lee, H. High-performance hybrid supercapacitor with 3D hierarchical porous flower-like layered double hydroxide grown on nickel foam as binder-free electrode. *J. Power Sources* **2016**, *318*, 76−85.

(34) Brousse, T.; Bélanger, D.; Long, J. W. To be or not to be pseudocapacitive? *J. Electrochem. Soc.* **2015**, *162*, A5185−A5189.

(35) Pu, J.; Tong, Y.; Wang, S.; Sheng, E.; Wang, Z. Nickel−cobalt hydroxide nanosheets arrays on Ni foam for pseudocapacitor applications. *J. Power Sources* **2014**, *250*, 250−256.

(36) Lv, Z.; Zhong, Q.; Bu, Y. Controllable synthesis of Ni-Co nanosheets covered hollow box via altering the concentration of nitrate for high performance supercapacitor. *Electrochim. Acta* **2016**, *215*, 500−505.

(37) Xu, J.; Ju, Z.; Cao, J.; Wang, W.; Wang, C.; Chen, Z. Microwave synthesis of nitrogen-doped mesoporous carbon/nickel-cobalt hydroxide microspheres for high-performance supercapacitors. *J. Alloys Compd.* **2016**, *689*, 489−499.

(38) Wang, T.; Zhang, S.; Yan, X.; Lyu, M.; Wang, L.; Bell, J.; Wang, H. 2-Methylimidazole-derived Ni−Co layered double hydroxide nanosheets as high rate capability and high energy density storage material in hybrid supercapacitors. *ACS Appl. Mater. Interfaces* **2017**, *9*, 15510−15524.

(39) Zhang, L.; Hui, K. N.; Hui, K. S.; Lee, H. Facile synthesis of porous CoAl-layered double hydroxide/graphene composite with enhanced capacitive performance for supercapacitors. *Electrochim. Acta* **2015**, *186*, 522−529.

(40) Bai, C.; Sun, S.; Xu, Y.; Yu, R.; Li, H. Facile one-step synthesis of nanocomposite based on carbon nanotubes and nickel-aluminum layered double hydroxides with high cycling stability for supercapacitors. *J. Colloid Interface Sci.* **2016**, *480*, 57−62.

(41) Li, X.; Zai, J.; Liu, Y.; He, X.; Xiang, S.; Ma, Z.; Qian, X. Atomically thin layered NiFe double hydroxides assembled 3D microspheres with promoted electrochemical performances. *J. Power Sources* **2016**, *325*, 675−681.

(42) Lv, L.; Xu, K.; Wang, C.; Wan, H.; Ruan, Y.; Liu, J.; Zou, R.; Miao, L.; Ostrikov, K.; Lan, Y.; Jiang, J. Intercalation of glucose in NiMn-layered double hydroxide nanosheets: An effective path way towards battery-type electrodes with enhanced performance. *Electrochim. Acta* 2016, 216, 35−43.

(43) Hatui, G.; Nayak, G. C.; Udayabhanu, G. One pot solvothermal synthesis of sandwich-like Mg Al layered double hydroxide anchored reduced graphene oxide: An excellent electrode material for supercapacitor. *Electrochim. Acta* 2016, 219, 214−226.

(44) Singh, D.; Choudhary, A.; Garg, A. Flexible and robust piezoelectric polymer nanocomposites based energy harvesters. *ACS Appl. Mater. Interfaces* 2018, 10, 2793−2800.

(45) Zhang, L.; Zhang, X.; Shen, L.; Gao, B.; Hao, L.; Lu, X.; Zhang, F.; Ding, B.; Yuan, C. Enhanced high-current capacitive behavior of graphene/CoAl-layered double hydroxide composites as electrode material for supercapacitors. *J. Power Sources* 2012, 199, 395−401.

(46) Tao, Y.; Ruiyi, L.; Tingting, Y.; Zaijun, L. Nickel/cobalt layered double hydroxide hollow microspheres with hydrangea-like morphology for high-performance supercapacitors. *Electrochim. Acta* 2015, 152, 530−537.

(47) Li, M.; Ma, K. Y.; Cheng, J. P.; Lv, D.; Zhang, X. B. Nickel−cobalt hydroxide nanoflakes conformal coating on carbon nanotubes as a supercapacitive material with high-rate capability. *J. Power Sources* 2015, 286, 438−444.

(48) Tang, Y.; Liu, Y.; Yu, S.; Guo, W.; Mu, S.; Wang, H.; Zhao, Y.; Hou, L.; Fan, Y.; Gao, F. Template-free hydrothermal synthesis of nickel cobalt hydroxide nanoflowers with high performance for asymmetric supercapacitor. *Electrochim. Acta* 2015, 161, 279−289.

(49) Li, R.; Hu, Z.; Shao, X.; Cheng, P.; Li, S.; Yu, W.; Lin, W.; Yuan, D. Large scale synthesis of NiCo layered double hydroxides for superior asymmetric electrochemical capacitor. *Sci. Rep.* 2016, 6, No. 18737.

(50) Lin, W.; Yu, W.; Hu, Z.; Ouyang, W.; Shao, X.; Li, R.; Yuan, D. S. Superior performance asymmetric supercapacitors based on flake-like Co/Al hydrotalcite and graphene. *Electrochim. Acta* 2014, 143, 331−339.

(51) Li, X.; Zhang, Y.; Xing, W.; Li, L.; Xue, Q.; Yan, Z. Sandwich-like graphene/polypyrrole/layered double hydroxide nanowires for high-performance supercapacitors. *J. Power Sources* 2016, 331, 67−75.

(52) Zhang, F.; Zhang, C.; Zeng, R.; Song, L.; Guo, L.; Huang, X. Corrosion resistance of the superhydrophobic Mg(OH)₂/Mg-Al layered double hydroxide coatings on magnesium alloys. *Metals* 2016, 6, 85.

(53) Hsieh, Z.-L.; Lin, M.-C.; Uan, J.-Y. Rapid direct growth of Li-Al layered double hydroxide (LDH) film on glass, silicon wafer and carbon cloth and characterization of LDH film on substrates. *J. Mater. Chem.* 2011, 21, 1880−1889.

(54) Masikhwa, T. M.; Madito, M. J.; Momodu, D. Y.; Dangbegnon, J. K.; Guellati, O.; Harat, A.; Guerioune, M.; Barzegar, F.; Manyala, N. High performance asymmetric supercapacitor based on CoAl-LDH/GF and activated carbon from expanded graphite. *RSC Adv.* 2016, 6, 46723−46732.

(55) Tan, Za.; Zhang, W.; Qian, D.; Cui, C.; Xu, Q.; Li, L.; Li, S.; Li, Y. Solution-processed nickel acetate as hole collection layer for polymer solar cells. *Phys. Chem. Chem. Phys.* 2012, 14, 14217−14223.

(56) De Jesus, J. C.; González, I.; Quevedo, A.; Puerta, T. Thermal decomposition of nickel acetate tetrahydrate: An integrated study by TGA, QMS and XPS techniques. *J. Mol. Catal. A: Chem.* 2005, 228, 283−291.

(57) Mansour, A. N. Characterization of NiO by XPS. *Surf. Sci. Spectra* 1994, 3, 231−238.

(58) Biesinger, M. C.; Payne, B. P.; Grosvenor, A. P.; Lau, L. W. M.; Gerson, A. R.; Smart, R. S. C. Resolving surface chemical states in XPS analysis of first row transition metals, oxides and hydroxides: Cr, Mn, Fe, Co and Ni. *Appl. Surf. Sci.* 2011, 257, 2717−2730.

(59) Biesinger, M. C.; Lau, L. W. M.; Gerson, A. R.; Smart, R. S. C. Resolving surface chemical states in XPS analysis of first row transition metals, oxides and hydroxides: Sc, Ti, V, Cu and Zn. *Appl. Surf. Sci.* 2010, 257, 887−898.

(60) Silversmit, G.; Depla, D.; Poelman, H.; Marin, G. B.; De Gryse, R. Determination of the V2p XPS binding energies for different vanadium oxidation states (V⁵⁺ to V⁰⁺). *J. Electron Spectrosc. Relat. Phenom.* 2004, 135, 167−175.

(61) Chen, H.; Deng, Y.; Yu, Z.; Zhao, H.; Yao, Q.; Zou, X.; Bäckvall, J.-E.; Sun, J. 3D open-framework vanadoborate as a highly effective heterogeneous pre-catalyst for the oxidation of alkylbenzenes. *Chem. Mater.* 2013, 25, 5031−5036.

(62) Hu, Z.-A.; Xie, Y.-L.; Wang, Y.-X.; Wu, H.-Y.; Yang, Y.-Y.; Zhang, Z.-Y. Synthesis and electrochemical characterization of mesoporous CoₓNi₁₋ₓ layered double hydroxides as electrode materials for supercapacitors. *Electrochim. Acta* 2009, 54, 2737−2741.

(63) Caravaggio, G. A.; Detellier, C.; Wronski, Z. Synthesis, stability and electrochemical properties of NiAl and NiV layered double hydroxides. *J. Mater. Chem.* 2001, 11, 912−921.

(64) Park, H. W.; Chae, J. S.; Park, S.-M.; Kim, K.-B.; Roh, K. C. Nickel-based layered double hydroxide from guest vanadium oxide anions. *Met. Mater. Int.* 2013, 19, 887−894.

(65) Zhao, J.; Chen, J.; Xu, S.; Shao, M.; Zhang, Q.; Wei, F.; Ma, J.; Wei, M.; Evans, D. G.; Duan, X. Hierarchical NiMn layered double hydroxide/carbon nanotubes architecture with superb energy density for flexible supercapacitors. *Adv. Funct. Mater.* 2014, 24, 2938−2946.

(66) Teh, P. F.; Sharma, Y.; Pramana, S. S.; Srinivasan, M. Nanoweb anodes composed of one-dimensional, high aspect ratio, size tunable electrospun ZnFe₂O₄ nanofibers for lithium ion batteries. *J. Mater. Chem.* 2011, 21, 14999−15008.

(67) Li, M.; Cheng, J. P.; Wang, J.; Liu, F.; Zhang, X. B. The growth of nickel-manganese and cobalt-manganese layered double hydroxides on reduced graphene oxide for supercapacitor. *Electrochim. Acta* 2016, 206, 108−115.

(68) Wang, X.; Sumboja, A.; Lin, M.; Yan, J.; Lee, P. S. Enhancing electrochemical reaction sites in nickel−cobalt layered double hydroxides on zinc tin oxide nanowires: A hybrid material for an asymmetric supercapacitor device. *Nanoscale* 2012, 4, 7266−7272.

(69) Jagadale, A. D.; Guan, G.; Li, X.; Du, X.; Ma, X.; Hao, X.; Abudula, A. Ultrathin nanoflakes of cobalt−manganese layered double hydroxide with high reversibility for asymmetric supercapacitor. *J. Power Sources* 2016, 306, 526−534.

(70) Lee, I.; Jeong, G. H.; An, S.; Kim, S.-W.; Yoon, S. Facile synthesis of 3D MnNi-layered double hydroxides (LDH)/graphene composites from directly graphites for pseudocapacitor and their electrochemical analysis. *Appl. Surf. Sci.* 2018, 429, 196−202.

(71) Huang, L.; Liu, B.; Hou, H.; Wu, L.; Zhu, X.; Hu, J.; Yang, J. Facile preparation of flower-like NiMn layered double hydroxide/reduced graphene oxide microsphere composite for high-performance asymmetric supercapacitors. *J. Alloys Compd.* 2018, 730, 71−80.

(72) Fan, K.; Chen, H.; Ji, Y.; Huang, H.; Claesson, P. M.; Daniel, Q.; Philippe, B.; Rensmo, H.; Li, F.; Luo, Y.; Sun, L. Nickel−vanadium monolayer double hydroxide for efficient electrochemical water oxidation. *Nat. Commun.* 2016, 7, No. 11981.

(73) Zhang, J.; Zhao, X. S. On the configuration of supercapacitors for maximizing electrochemical performance. *ChemSusChem* 2012, 5, 818−841.

(74) Shen, P.; Zhang, H.; Zhang, S.; Fei, L. Fabrication of completely interface-engineered Ni(OH)₂/rGO nanoarchitectures for high-performance asymmetric supercapacitors. *Appl. Surf. Sci.* 2018, 460, 65−73.

(75) Long, J. Y.; Yan, Z. S.; Gong, Y.; Lin, J. H. MOF-derived Cl/O-doped C/CoO and C nanoparticles for high performance supercapacitor. *Appl. Surf. Sci.* 2018, 448, 50−63.

(76) Wang, N.; Wang, Y.; Cui, S.; Hou, H.; Mi, L.; Chen, W. A hollow tube-on-tube architecture of carbon-tube-supported nickel cobalt sulfide nanotubes for advanced supercapacitors. *ChemNanoMat* 2017, 3, 269−276.

(77) Rong, H.; Chen, T.; Shi, R.; Zhang, Y.; Wang, Z. Hierarchical NiCo₂O₄@NiCo₂S₄ nanocomposite on Ni foam as an electrode for hybrid supercapacitors. *ACS Omega* 2018, 3, 5634−5642.

(78) Fang, Z.; Rehman, Su.; Sun, M.; Yuan, Y.; Jin, S.; Bi, H. Hybrid NiO−CuO mesoporous nanowire array with abundant oxygen

vacancies and a hollow structure as a high-performance asymmetric supercapacitor. *J. Mater. Chem. A* **2018**, *6*, 21131−21142.

(79) Liu, T.; Zhang, L.; You, W.; Yu, J. Core−shell nitrogen-doped carbon hollow spheres/Co_3O_4 nanosheets as advanced electrode for high-performance supercapacitor. *Small* **2018**, *14*, No. 1702407.

(80) Hu, H.; Guan, B.; Lou, X. W. Construction of complex CoS hollow structures with enhanced electrochemical properties for hybrid supercapacitors. *Chem* **2016**, *1*, 102−113.

2019-02-14

Hydrothermally tailored three-dimensional Ni-V layered double hydroxide nanosheets as high-performance hybrid supercapacitor applications

Tyagi, Ankit